Thermal and optical performance analysis of triangular solar air collectors and regional applicability in China

Yan Jiang [a, b], Huan Zhang [a, b], Rui Zhao [a, b], Zhikai Liu [a, b], Yaran Wang [a, b, *], Shijun You [a, b], Zhangxiang Wu [a, b], Shen Wei [c]

[a] School of Environmental Science and Engineering, Tianjin University, Haihe Education Area, Jinnan District, Tianjin 300350, PR China

[b] Tianjin Key Lab of Biomass/Wastes Utilization, Tianjin 300350, PR China

[c] The Bartlett School of Construction and Project Management, University College London (UCL), 1-19 Torrington Place, London WC1E 7HB, United Kingdom

Abstract

Improving the applicability of solar air collectors in different climatic regions is important for its popularization. In this study, a novel triangular solar air collector (TSAC) was proposed. The insulation material (TSAC_1), transparent cover plate (TSAC_2) or double transparent cover plate (TSAC_3) could be fitted on the side of TSAC to adapt to different climates. The optical model and heat transfer model of the TSACs were established and verified. Two optical efficiencies were defined and the optical properties of three TSACs were compared. The effect of environment temperature, global solar radiation, solar azimuth angle and insulation material absorption on the thermal performance of TSACs were analyzed. Based on meteorological parameters of eight cities in different climate and solar energy

[*] *Corresponding author. Tel.: +8602227892626; fax: +8602227892626.*

E-mail addresses: yaran_wang@tju.edu.cn

distribution regions, the applicability of TSACs was compared, and their life-cycle economics and CO_2 emission reduction capacity were assessed. Results indicate that the TSAC_2 has the highest optical efficiency, and 15.2% higher than that of TSAC_1. Three TSACs are suitable for different climatic regions, the average thermal efficiency of the optimal TSAC applied to the eight cities is 47.3% during the heating period, which is 5.6% higher than that of the single TSAC_1. TSACs have good economics in all climate regions, and the average net CO_2 emission reduction of whole life cycle is 3230.3 kg.

Keywords:

solar space heating; solar air collector; optical model; heat transfer model; economic evaluation

Nomenclature		dif	diffuse radiation
A	surface area (m^2)	env	environment
c	heat capacity (W/K)	g	ground
c_p	specific heat capacitance (J/(kg·K))	gc	glass cover
		hole	hole of perforated corrugated
EF_{pro}	CO_2 emission factors of Production(kg/kg)	in	inlet
		ins	insulation housing
EF_{tran}	CO_2 emission factors of transportation(kg/kg)	insr	right insulation housing
		insl	left insulation housing
h	solar altitude(°)	out	outlet
I	solar irradiance (W/m^2)	sol	solar
I_g	global solar irradiance (W/m^2)	t	thermal
I_{year}	the total annual radiation(MJ/m^2)	tcp	transparent cover plate
ie	the effective interest rate (%)	*Greek*	
if	inflation rate (%)	*symbols*	
m	mass flow rate (kg/s)	α	absorptivity (-)
n	beneficial years	β	solar azimuth(°)
q	Energy(W)	ε	emissivity (-)
Q_{air}	heat collection	η_o	optical efficiency (%)
S	absorbed solar radiation	η_t	thermal efficiency (%)
T	temperature (℃)	λ	heat conductivity coefficient (W/m/K)
T_{min}	the average temperature of the coldest month (℃)	θ	inclination angle (°)
v	specific volume (m^3/kg)	τ	transmissivity (-)
V	volume	*Abbreviations*	
Subscripts		FVM	Finite Volume Method
ab	perforated corrugated absorber	MCM	Monte Carlo Method
air	circulating air of TSAC	SAC	solar air collector

conv d	convection heat transfer direct	TSAC	triangular solar air collector

1. Introduction

Solar thermal utilization is one of the main solar energy technologies, and according to the data of the International Renewable Energy Agency (IRENA), the world's total installed capacity of solar thermal utilization reached 6387 MW in 2021 (IRENA, 2022). Solar thermal utilization technology can be applied to power generation, space heating, crop drying and providing domestic hot water, and solar space heating is considered to have great development potential (Zhao et al., 2015). In China, the building area of solar space heating has reached 50 million m^2 in 2021, about 4 times of that in 2020, and the area of solar collector for space heating has reached 10 million m^2 (CNEA, 2022).

Solar collectors can be divided into solar water collectors and solar air collectors (SAC), compared with the solar water collector, SAC has the following advantages (Dong et al., 2021; Zhao et al., 2020) for space heating: (1) SAC can directly heat the space without an additional radiator, and the SAC system is simple and economical. (2) The heat transfer medium of SAC is air and does not require anti-freezing measures. (3) SAC is easy to operate and responds faster. (4) The solar water collector requires a pump to operate, while SAC can circulate air through natural convection or a low-power fan. (5) SAC can be integrated with the building as a thermal insulation component of the envelope. For the above reasons, SAC is suitable for space heating, especially for rural residences that seek economy. (6) SAC can help ventilate the building during the non-heating season.

The disadvantage of SAC is the low thermal efficiency, as the heat capacity and convective heat transfer coefficient of circulating air are small. Enhancing heat transfer is the main way to improve the thermal performance of SAC, and changing the structure of heat absorber to promote turbulence is a common means (Vengadesan and Senthil, 2020; Khanlari et al., 2021a). Rani and Tripathy et al. (2022) add baffle on the absorber at the air inlet to evenly distribute the air flow, and install hollow semicircular loops on the whole absorber to improve the heat exchange efficiency with circulating air, and compared with the smooth absorber, the thermal efficiency is increased by 19.73%. Khanlari. et al. (2021b) found that parallel-flow SAHWs (solar air heating walls) exhibited better performance in comparison with other placements of absorber plate, and the highest thermal efficiency is reach to 80.51%. Chand et al. (2022) construct the SAC with louvered fins and perform experiments to evaluate its thermal performance, and the maximum thermal efficiency of novel SAC can reach 70%. Compared with the installation of turbulence components for the absorber, the transpired absorber with perforated surface has a simple structure and can significantly improve the heat transfer efficiency (Gao et al., 2020). Bejan et al. (2022) consider transpired SAC to be a low-cost, high-efficiency system suitable for building heating. Zhang et al. (2018) and Zheng et al. (2016) analyzed the performance of transpired SAC with slit-perforated corrugated absorber and hole-perforated corrugated absorber, and their maximum thermal efficiency was about 65% and 70%, respectively. In addition to the surface modification of the absorber, the heat transfer of SAC can also be enhanced by increasing the heat transfer area of the absorber and the circulating air (Tuncer et al.,

2020). Dong et al. (2021) designed a double-channel SAC, and circulating air can simultaneously exchange heat with the upper and lower surfaces of the absorber. Kareem et al. (2022) proposed a quadruple-pass SAC to achieve sufficient heat transfer, and the mean thermal efficiency is in the range of 71.63% to 80.66%. Another way to improve the thermal performance of the SAC is to reduce the heat loss of the transparent cover plate and the environment. Marc et al. (2011) adopted double transparent cover plate to enhance the greenhouse effect of the collector. Kizildag et al. (2022) demonstrated a highly efficient SAC based on transparent insulation technology and the energy collected is about 2.5 times higher than conventional SAC in winter. The recent studies are based on flat SAC, while there are few researches on changing SAC geometry structure to improve its thermal performance.

Environmental parameters such as solar radiation and outdoor temperature are the key parameters affecting the performance of SAC, as it is necessary to study the applicability of SAC in different climatic regions. Ke et al. (2021) calculated the annual operating performance of a dual-air-channel SAC in three cities, and the average thermal efficiency difference is about 2%. Zhang et al. (2019) proposed a SAC as a fresh air preheating system for buildings, and the results show that the thermal performance of the system is mainly affected by solar radiation, and the system has the greatest energy saving potential in Lhasa. Studies of SAC in different climatic regions are limited to analyzing its applicability, and there is no modification of SAC structure to operate efficiently in all climatic regions.

In addition, optical model is very important for the analysis of solar collector

performance. Based on the calculation method of the solar ray position, optical model can be divided into Monte Carlo Method (MCM) and Finite Volume Method (FVM). Ramasamy et al. (2021) proposed a concentrated solar collector combining Parabolic Trough Concentrators and Linear Fresnel Concentrators, and analyzed its optical performance under shading and blocking based on MCM method. Rehman et al. (2018) optimized MCM based on Latin-Hypercube sampling technique and established an optical model of solar collector with a flat booster reflector. Liang et al. (2018) compared MCM and FVM optical models of a parabolic trough solar collector, and the results show that the FVM is more efficient and stable, but it needs mesh generation. The study of optical model is mainly focused on the solar collector with concentrator or booster reflector, while the optical model of flat-plate solar collector is rarely reported. Fan et al. (2019) established an optical model of flat-plate solar collector based on the MCM and calculated the inter reflection and absorption of incident solar rays in the V-corrugated absorber. While the calculation results of MCM are fluctuating due to the influence of random number generation, as it is necessary to generate a large number of random numbers to improve the calculation accuracy, which consumes the calculation time. In contrast, FVM is more advantageous for flat-plate solar collectors without complex structure.

In summary, the SAC is suitable for space heating of rural residences, and can effectively improve the indoor thermal comfort of rural residents. The SAC is usually installed on the south wall of the building, but the windows and doors in Chinese rural residences are designed on the south wall, which leads to the limited area available for

installing the SAC.

In view of these, a novel triangular solar air collector (TSAC) is proposed, it has a tilted transparent cover plate on the front and also can be fitted with the transparent cover plate on the side to receive more solar radiation. The TSAC dynamic heat transfer model and the optical model based on FVM were established and validated by experiments. Three different materials including insulation material, single transparent cover plate, and double transparent cover plate are applied on sides of the TSAC to adapt to different climate regions. The main contributions of this study include three parts: (1) A novel TSAC with three different side materials was proposed. (2) Based on the FVM, a novel 3D optical model for non-concentrating solar collector was established, and two kinds of TSAC optical efficiency were defined and compared. (3) The applicability of three TSACs in different climatic and solar energy distribution regions was analyzed based on heating capacity, economy and environmental impact.

2. Methods

2.1. Geometric and physical model

TSAC structure and absorber photograph are shown in Fig. 1. The recirculating air enters the TSAC through the air inlet, exchanges heat with the absorbers, and then exits through the air outlet. The surfaces of the absorbers are coated with black chromium deposition to improve the solar absorption. The inclination angle of the front transparent cover plate is 60^{o}, which is the best inclination angle of solar collector in winter. The inclination angles of the absorbers from top to bottom are 30°, 120°, and 52° to ensure that the three absorbers don't block each other during the whole heating

season (Jiang et al., 2021). The back and underside materials of the TSAC are insulation housing, but the side materials can be selected as insulation housing (TSAC_1), single transparent cover plate (TSAC_2) or double transparent cover plate (TSAC_3) according to local weather parameters. Compared with traditional flat-plate solar air collector, TSAC has the following advantages :(1) The inclined front transparent cover plate can receive more solar radiation; (2) The area of the absorber is larger, and the heat transfer with the recirculating air is strengthened; (3) The triangle structure is stable and easy to install. The geometric and physical parameters of the TSAC are shown in Table 1.

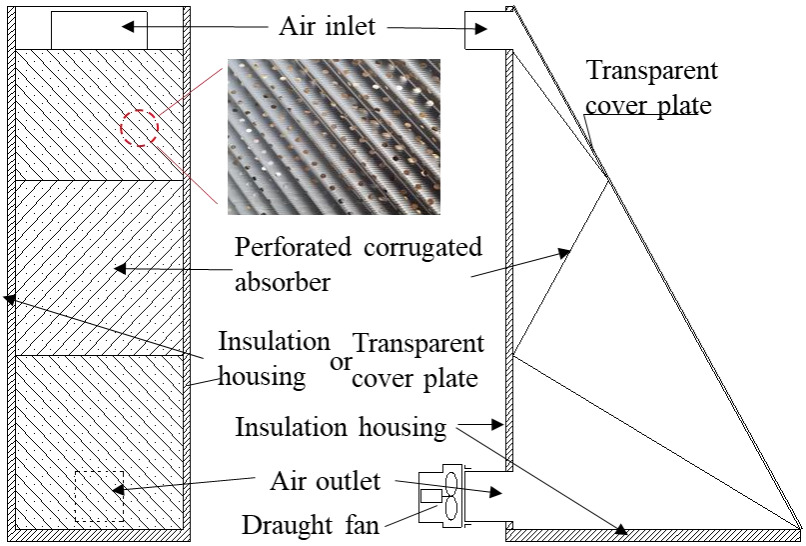

Fig. 1. Structure of the TSAC

Table. 1. The geometric and physical parameters of the TSAC.

TSAC	Section size: 2.4×2.1×1.2 (m×m×m), width: 0.7 (m)
Single/Double transparent cover plate	Materials: Polycarbonate; Physical parameter: α_{tcp}=0.1; ε_{tcp}=0.67; λ_{tcp}=0.2/0.06 (W/(m·K)); τ_{tcp}=0.89/0.79;
Perforated corrugated absorber	Materials: Stainless steel, Thickness:0.15 mm Physical parameter: λ_{ab}=14.8 (W/(m·K)); α_{ab}=0.92; ε_{ab}=0.2;

Insulation housing	Materials: Polystyrene board and galvanized sheet Physical parameter: λ_{ins}=0.028 (W/(m·K)); α_{ins}=0.2; ε_{ins}=0.1
Air inlet/outlet	Section size: 0.15×0.4/0.2×0.2 (m×m), length: 0.6 (m)

2.2. Optical model

The optical model of TSAC is established based on FVM, and the following assumptions are considered to facilitate (Fan et al., 2019). (1) As TSAC is the non-concentrating solar collector, the solar half cone angel is ignored, and the incident rays are parallel. (2) The optical properties of TSAC components remain constant with the change of solar incident angle (the incident angle in this paper is based on the front transparent cover plate). (3) As the transparent cover plate is thin, the refraction of the transparent cover plate to the incident rays is ignored. (4) Diffuse radiation entering the TSAC from the transparent cover plate is evenly distributed on the visible surface of TSAC. (5) Incident rays escaping from air inlet and outlet are ignored.

Fig. 2 shows the sketch of the optical model for TSAC. The origin of the coordinate system is at the midpoint of the intersection between the TSAC back and the bottom surface, and the unit vector of solar incident rays $\vec{m}$ at any time is calculated as follows:

$$x_{\mathrm{sol}} = \cos(h) \times \sin(\beta) \tag{1}$$

$$y_{\mathrm{sol}} = -\sin(\beta) \tag{2}$$

$$z_{\mathrm{sol}} = -\left|\cos(h) \times \cos(\beta)\right| \tag{3}$$

A virtual surface is created to determine the starting positions of the solar incident rays, as presented in Fig. 2. A plane perpendicular to the Z-axis is established in the south of TSAC, and the intersection of the plane with the inverse extension line of the

incident ray passing through TSAC vertex is calculated. The maximum and minimum values of the x and y coordinates of the six intersections are selected and rectangular virtual surface is generated. The coordinates of the intersections are calculated as follows:

$$x_i' = x_i - \frac{(z_i - z_i')}{z_{\text{sol}}} \times x_{\text{sol}} \tag{4}$$

$$y_i' = y_i - \frac{(z_i - z_i')}{z_{\text{sol}}} \times y_{\text{sol}} \tag{5}$$

$$z_i' = \text{C} \tag{6}$$

A grid is generated for the rectangular virtual surface based on the number of solar incident rays. The grid nodes are the starting positions of rays, and the initial energy of each ray is calculated as follows:

$$q_{\text{ray}} = I_{\text{d}} \times \text{-}z_{\text{sol}} \times A_{\text{vir}} / N_{\text{rays}} \tag{7}$$

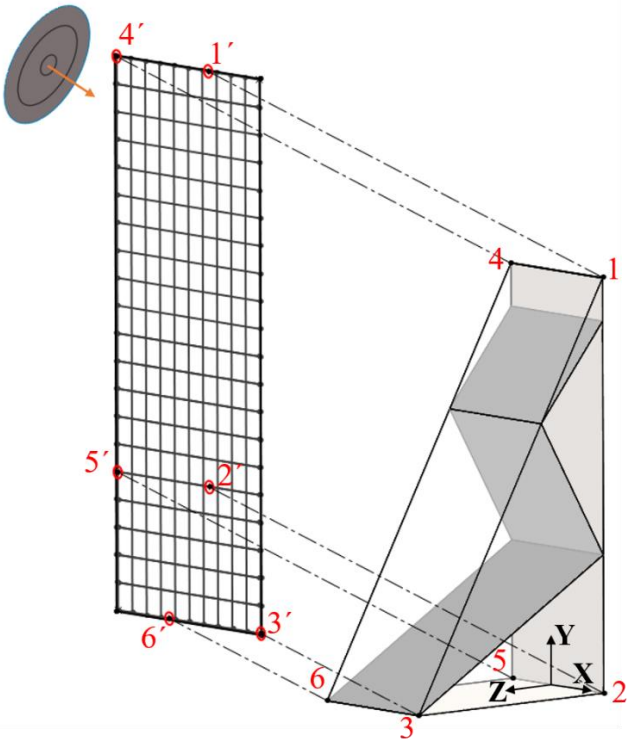

Fig. 2. Sketch of the optical model for TSAC

The equations of the solar incident rays emitted by the virtual surface and the TSAC surface can be expressed as follows, and $\vec{n}$ is the normal vector of the calculated TSAC surface:

$$\frac{x-x'}{x_{\text{sol}}}=\frac{y-y'}{y_{\text{sol}}}=\frac{z-z'}{z_{\text{sol}}}=l \tag{8}$$

$$\begin{bmatrix} x-x_i \\ y-y_i \\ z-z_i \end{bmatrix} \bullet \vec{n}=0 \tag{9}$$

The proportionality coefficient l of the incident ray equation is calculated by the above two equations.

$$l=\frac{\vec{n}\cdot\begin{bmatrix} x_i-x' \\ y_i-y' \\ z_i-z' \end{bmatrix}}{\vec{n}\cdot\vec{m}} \tag{10}$$

The proportionality coefficient is input the Eq.(8) and the intersection points between incident rays and TSAC surface are calculated, and select the real intersection point according to the size of the proportionality coefficient and the vertex coordinates of TSAC. The incident rays that intersect the surface of the TSAC are traced and if the side materials of the TSAC are insulation housing, only the incident rays that intersect the front transparent cover plate are traced.

The rays entering the TSAC through the transparent cover plate are reflected multiple times on the inner surface of the TSAC, and the reflections of rays are calculated according to Fresnel effect as follows:

$$\vec{r}=\vec{m}-2(\vec{m}\cdot\vec{n})\cdot\vec{n} \tag{11}$$

The calculation method of real intersection points between reflected rays and the

TSAC internal surface is the same as that of incident rays. The rays intersect the outer or inner surface of the TSAC, and the energy change of the rays and radiation received by the local TSAC surface are calculated considering the transmission, reflection and absorption processes.

The diffuse radiation generally accounts for 15% of the total radiation, and the diffuse radiation through the transparent cover plate is calculated as follows:

$$q_{\mathrm{dif}} = I_{\mathrm{dif}} \times \frac{1+\cos(\theta)}{2} \times A_{\mathrm{tcp}} \times \tau_{\mathrm{tcp}} \tag{12}$$

Assuming that the diffuse radiation entering the TSAC is evenly distributed on the visible surface of the TSAC, and multiple reflections of diffuse rays are ignored as the diffuse radiation received by each TSAC surface is only the local absorption rate.

2.3. Heat transfer model

The dynamic heat transfer model of the TSAC is established and the grid is generated along the Y-axis. The thermal properties of the TSAC components are considered fixed, and the circulating air is assumed to be an incompressible fluid (Jiang et al., 2022). The convective and radiative heat transfer of the TSAC including the heat transfer between circulating air, transparent cover plate, absorber and insulation housing, as well as transparent cover plate and environment are considered. The heat conduction of the circulating air along the flow direction is ignored, and its energy conservation equation can be written as follows:

$$\begin{aligned} m_{\mathrm{air}} c_{\mathrm{p.air}} \frac{\partial T_{\mathrm{air}}}{\partial \tau} + m_{\mathrm{air}} c_{\mathrm{p.air}} \frac{\partial (v_{\mathrm{air}} T_{\mathrm{air}})}{\partial y} = q_{\mathrm{conv.ins\text{-}air}} + q_{\mathrm{conv.hole}} + q_{\mathrm{conv.tcpf\text{-}air}} \\ + q_{\mathrm{conv.tcpl\text{-}air}} + q_{\mathrm{conv.tcpr\text{-}air}} + q_{\mathrm{conv.ab\text{-}air}} \end{aligned} \tag{13}$$

The energy conservation equations of the front and side transparent cover plates,

absorber and insulation housing are as follows:

$$m_{\text{tcpf}} c_{\text{p.tcpf}} \frac{\partial T_{\text{tcpf}}}{\partial \tau} = V_{\text{tcpf}} \lambda_{\text{tcpf}} \frac{\partial^2 T_{\text{tcpf}}}{\partial y^2} + s_{\text{tcpf}} + q_{\text{conv.tcpf-air}} + q_{\text{rad.tcpf-ab}} + q_{\text{rad.tcpf-ins}} + q_{\text{conv.tcpf-env}} + q_{\text{rad.tcpf-env}} \tag{14}$$

$$m_{\text{tcpl}} c_{\text{p.tcpl}} \frac{\partial T_{\text{tcpl}}}{\partial \tau} = V_{\text{tcpl}} \lambda_{\text{tcpl}} \frac{\partial^2 T_{\text{tcpl}}}{\partial y^2} + s_{\text{tcpl}} + q_{\text{conv.tcpl-air}} + q_{\text{conv.tcpl-env}} + q_{\text{rad.tcpl-env}} \tag{15}$$

$$m_{\text{tcpr}} c_{\text{p.tcpr}} \frac{\partial T_{\text{tcpr}}}{\partial \tau} = V_{\text{tcpr}} \lambda_{\text{tcpr}} \frac{\partial^2 T_{\text{tcpr}}}{\partial y^2} + s_{\text{tcpr}} + q_{\text{conv.tcpr-air}} + q_{\text{conv.tcpr-env}} + q_{\text{rad.tcpr-env}} \tag{16}$$

$$m_{\text{ab}} c_{\text{p.ab}} \frac{\partial T_{\text{ab}}}{\partial \tau} = V_{\text{ab}} \lambda_{\text{ab}} \frac{\partial^2 T_{\text{ab}}}{\partial y^2} + s_{\text{ab}} + q_{\text{conv.ab-air}} + q_{\text{conv.hole}} + q_{\text{rad.ab-tcp}} + q_{\text{rad.ab-ins}} + q_{\text{rad.ab-ab}} \tag{17}$$

$$m_{\text{ins}} c_{\text{p.ins}} \frac{\partial T_{\text{ins}}}{\partial \tau} = V_{\text{ins}} \lambda_{\text{ins}} \frac{\partial^2 T_{\text{ins}}}{\partial y^2} + s_{\text{ins}} + q_{\text{conv.ins-air}} + q_{\text{rad.ins-tcp}} + q_{\text{rad.ins-ab}} + q_{\text{rad.ins-ins}} \tag{18}$$

If the side material of TSAC is insulation housing, the energy conservation equations of the circulating air and side insulation housing are as follows:

$$m_{\text{air}} c_{\text{p.air}} \frac{\partial T_{\text{air}}}{\partial \tau} + m_{\text{air}} c_{\text{p.air}} \frac{\partial (v_{\text{air}} T_{\text{air}})}{\partial y} = q_{\text{conv.ins-air}} + q_{\text{conv.hole}} + q_{\text{conv.tcpf-air}} + q_{\text{conv.insl-air}} + q_{\text{conv.insr-air}} + q_{\text{conv.ab-air}} \tag{19}$$

$$m_{\text{insl}} c_{\text{p.insl}} \frac{\partial T_{\text{insl}}}{\partial \tau} = V_{\text{insl}} \lambda_{\text{insl}} \frac{\partial^2 T_{\text{insl}}}{\partial y^2} + s_{\text{insl}} + q_{\text{conv.insl-air}} \tag{20}$$

$$m_{\text{insr}} c_{\text{p.insr}} \frac{\partial T_{\text{insr}}}{\partial \tau} = V_{\text{insr}} \lambda_{\text{insr}} \frac{\partial^2 T_{\text{insr}}}{\partial y^2} + s_{\text{insr}} + q_{\text{conv.insr-air}} \tag{21}$$

The discrete methods of diffusion, convective and unsteady terms are central difference, first-order upwind and fourth-order Runge-Kutta respectively, and the calculation method of the other heat transfer terms in the energy conservation equations are presented in our previous study (Jiang et al., 2021).

2.4. Numerical method

The boundary conditions of the optical model and heat transfer model include local longitude and latitude, local time, solar direct radiation, solar diffuse radiation,

environment temperature, wind speed, inlet temperature and flow rate of circulating air. The local latitude, longitude and time are used to calculate the unit vector of solar incident rays and determine the virtual surface and ray starting positions. Eqs. 8~10 are solved to obtain the intersection points of the rays and the TSAC. The energy absorbed by each TSAC grid is recorded, and the unit vectors and energy of rays are updated. Multiple reflections are calculated until the energy of rays is below the threshold. The diffuse radiation and total radiation absorbed by each grid of the TSAC are calculated and input into the heat transfer model. The temperatures of the transparent cover plate, absorber and insulation housing are assumed to obtain the coefficients associated with them, and the heat transfer model is solved to derive their calculated values. The temperatures are calculated iteratively until the calculation converges, and the calculation of the next time step begins. The numerical method is realized by Python environment and the flowchart of the numerical method is shown in Fig. 3.

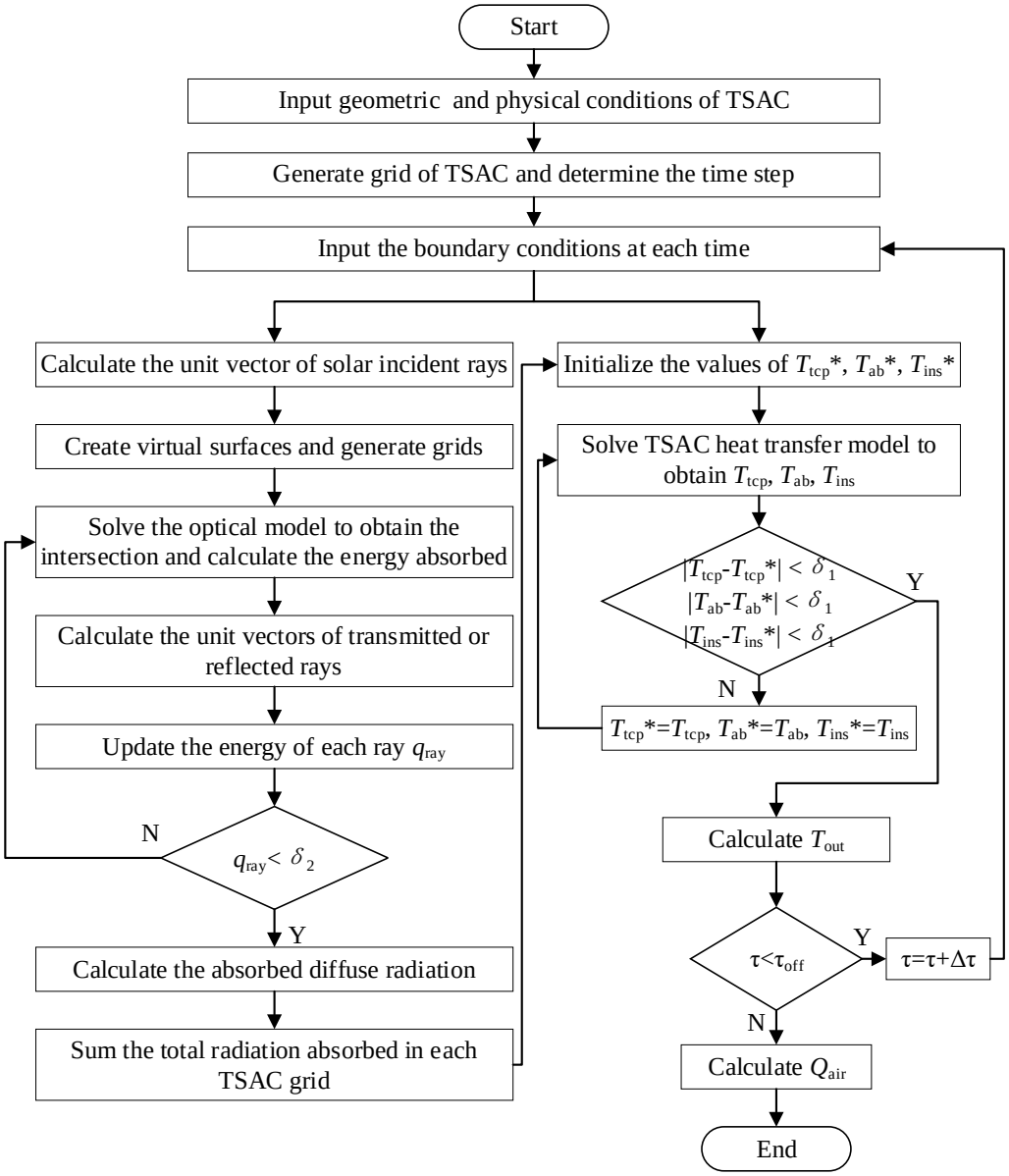

Fig. 3. Flowchart of the numerical method

2.5. Evaluation indices

To evaluate the performance of TSAC, the optical efficiency, thermal efficiency, and heat collection of the TSAC are defined. Optical efficiency is the absorbed proportion of the total solar radiation on the solar collector surface. For traditional solar collectors, the solar radiation is mainly absorbed by the absorber, while for TSAC with transparent cover plates on both sides, the solar radiation absorbed by insulation materials and transparent cover plates are also considered. The two optical efficiencies

are defined as follows:

$$\eta_{o1} = \frac{S_{ab}}{\sum A_{tcp} I_g} \tag{22}$$

$$\eta_{o2} = \frac{S_{ab} + S_{tcp} + S_{ins}}{\sum A_{tcp} I_g} \tag{23}$$

Thermal efficiency indicates the potential of TSAC to convert solar energy into the heat collection. The thermal efficiency and heat collection can be derived as:

$$\eta_t = \frac{m_{air} c_{p.air} \Delta T_{air}}{\sum A_{tcp} I_g} \tag{24}$$

$$Q_{air} = \int m_{air} c_{p.air} \Delta T_{air} d\tau \tag{25}$$

The life-cycle cost (*LCC*) is an important index to evaluate the TSAC economy (Fan et al., 2019), considering the initial cost (*IC*), operation cost (*OPC*), maintenance cost (*MC*) and salvage value (*SV*). The levelized cost of heating (*LCOH*) indicates the heating price of the TSAC in its whole life-cycle, which transforms the annual heat collection (AQ_{air}) into the present value. The *LCC* and *LCOH* are calculated as follows:

$$LCC = IC + MC \frac{(1+ie)^n - 1}{ie(1+ie)^n} + OPC \frac{(1+ie)^n - 1}{ie(1+ie)^n} - SV \frac{1}{(1+ie)^n} \tag{26}$$

$$LCOH = LCC / \left(AQ_{air} \frac{(1+ie)^n - 1}{ie(1+ie)^n} \right) \tag{27}$$

The TSAC used for space heating can save energy consumption for building heating and reduce CO_2 emissions ($RTCO_2$). While the TSAC also generates CO_2 emissions in the process of production ($EPCO_2$), transportation ($ETCO_2$) and dismantling ($EDCO_2$), as well as the electric consumption of fans during operation ($EECO_2$). It is necessary to calculate the net CO_2 emissions reduced ($RNCO_2$) of TSAC in the whole life cycle as follows:

$$RNCO_2 = RTCO_2 - EPCO_2 - ETCO_2 - EDCO_2 - EECO_2 \quad (28)$$

The calorific value of standard coal is about 29.271MJ/kg, and its CO_2 emission factor is 2.5, as the CO_2 emission reduced by TSAC in the whole life cycle is calculated as follows:

$$RTCO_2 = \frac{AQ_{\text{air}} \times n}{29.271 \times 10^6} \times 2.5 \quad (29)$$

The $EPCO_2$ and $ETCO_2$ are calculated with the TSAC's material mass and its corresponding CO_2 emission factor, the $EDCO_2$ is one-tenth of the $EPCO_2$.

3. Experiments

3.1. Experimental system

The experimental rigs for two types of TSAC are set up in Tianjin, China (38.98ºN, 117.38ºE). The sketch and photograph of experimental rig are depicted in Fig. 4. The thermostatic air tank is used to provide a specified inlet temperature and the draught fan drives the circulating air. During the test, the inlet temperature, outlet temperature and air flow of the circulating air were measured at the position shown in the sketch of experiment rig. The solar total radiation, solar diffuse radiation, environment temperature and wind speed were monitored and recorded every 5 seconds. The parameters of measuring instruments are shown in Table 2. The two experiments were completed during the local heating period, the TSAC_1 was tested in January 26, and the TSAC_2 was tested in March 15. The solar radiation of both experimental days was about 800 W/m^2, and the environment temperature on March 15 was about 11 ℃ and that on January 26 was 5 ℃.

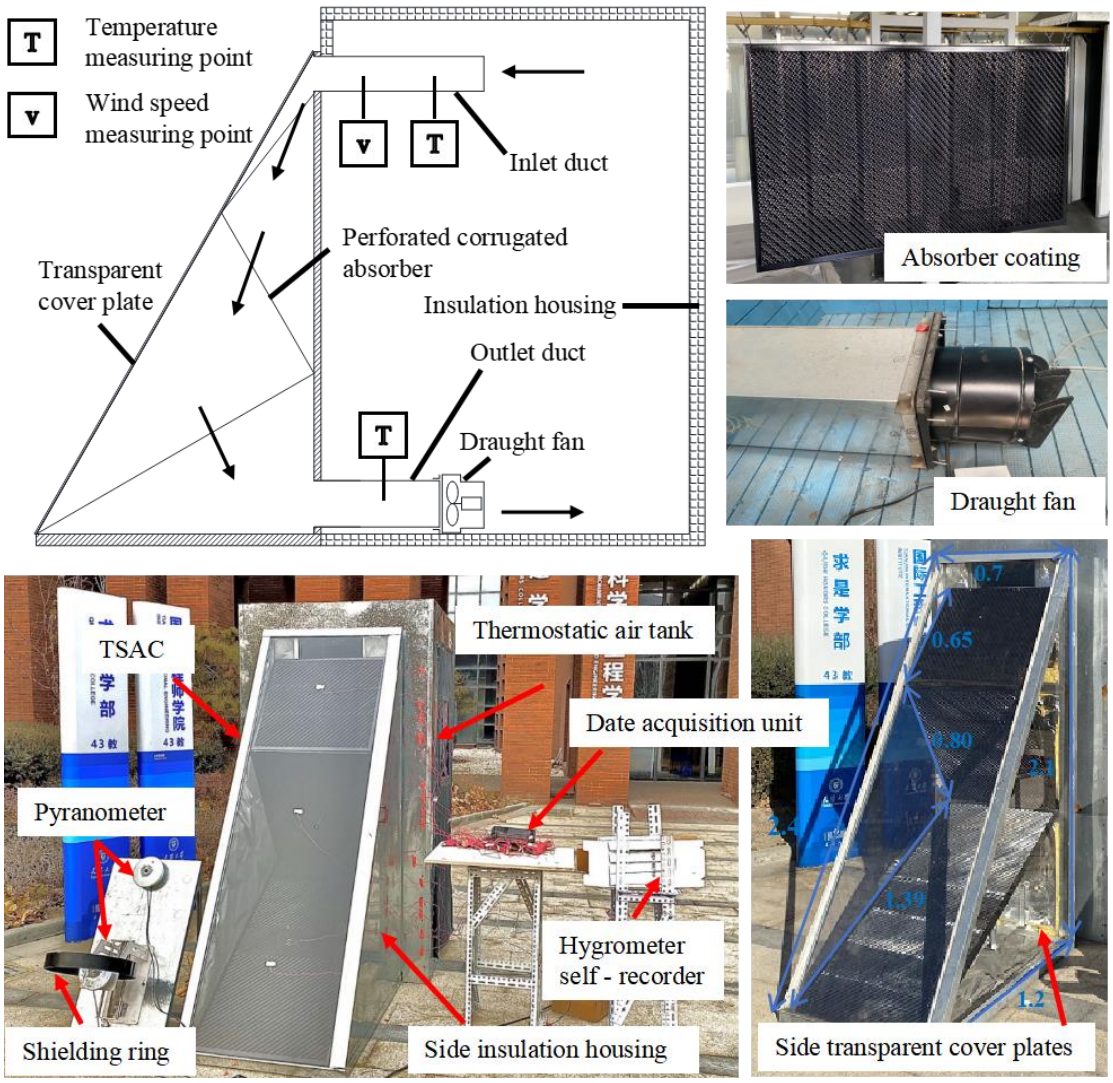

Fig. 4. Sketch and photograph of experimental rig for TSAC

Table. 2. Brand, model, range and accuracy values of measuring instruments.

Parameter	Instrument	Brand and model	Range	Accuracy
T_{in}, T_{out}	Thermocouple	T-type	-50 ~ 150 ℃	±0.5 ℃
v_{in}	Hotwire probe	Testo-405i	0 ~ 30 m/s	±0.1 m/s
T_{env}	Thermometer and hygrometer self - recorder	Testo-175H1	-35 ~ 150 ℃	±0.5 ℃
v_{env}	Totwire probe	Testo-405i	0 ~ 30 m/s	±0.1 m/s
I_g, I_d	Pyranometer	TBQ-2-B	0 ~ 1400 W/m^2	±2%

3.2. Experimental results and model validation

The gird number of the virtual surface and the TSAC affect the calculation accuracy of the optical and heat transfer model, hence, a gird independence check is carried out. The absorbers are the main component receiving solar radiation. The calculated values of the absorber receiving the solar radiation under different virtual surface grid numbers are presented in Fig. 5 (a). The calculated difference between the absorber receiving solar radiation with a grid number of 1,000,000 and 4,000,000 is less than five thousandths, and the calculation time of the former is only one-third of the latter, thus the virtual surface grid number of 1000,000 is regarded as accurate and efficient. Fig. 5(b) shows the calculated values of circulating air outlet temperature with different TSAC grid numbers. The heat collection difference between 2500 and 3000 girds is less than 3%, as the TSAC grid number of 2500 is selected.

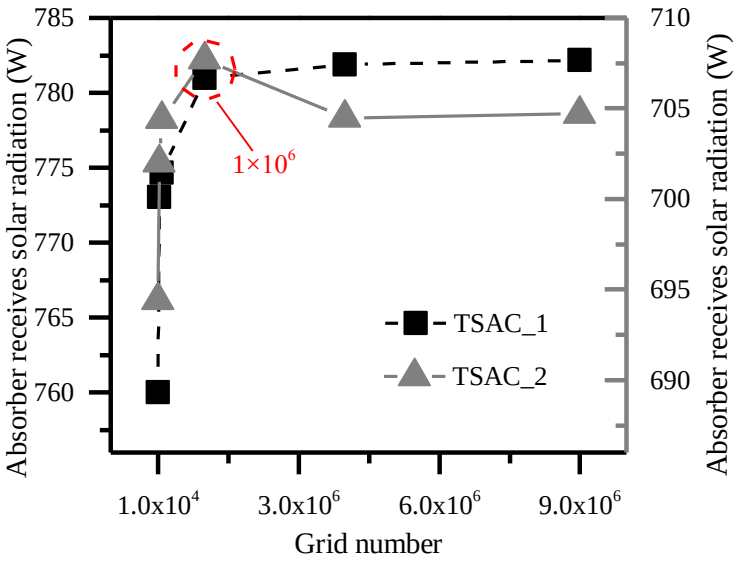

(a)

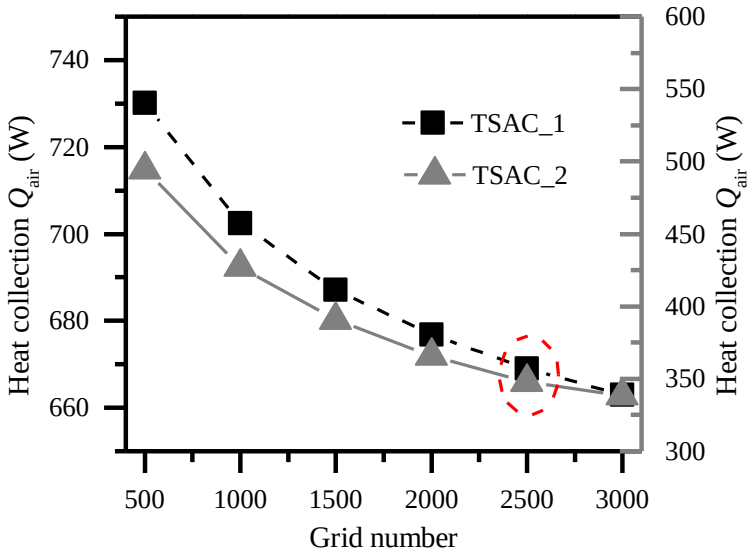

(b)

Fig. 5. The grid independence check for optical and heat transfer model

The temperature rise of circulating air and heat collection are the main indexes to evaluate the performance of the TSACs, and Fig.6 (a) and (b) show these two indexes of TSAC_1 and TSAC_2 at different air mass flow, respectively. The maximum errors of the temperature rise and the heat collection for the TSAC_1 are 0.7 ℃ and 67.3 W, and the average relative errors are 4.6%. The average and maximum relative errors of the heat collection for TSAC_2 are 7.0% and 9.8%. The average uncertainty of the heat collection during the test is 12.3%. Therefore, the tested and predicted values for temperature rise and heat collection indicate satisfactory consistencies, which shows the reliability of the presented TSAC optical and heat transfer model.

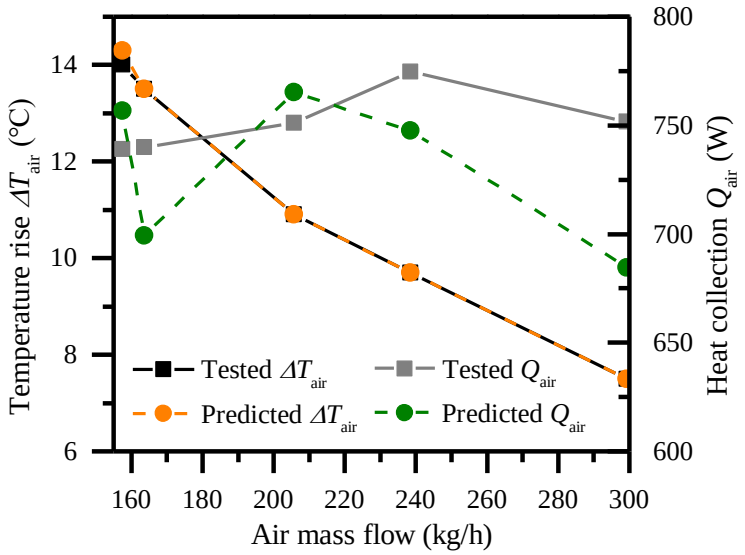

(a)

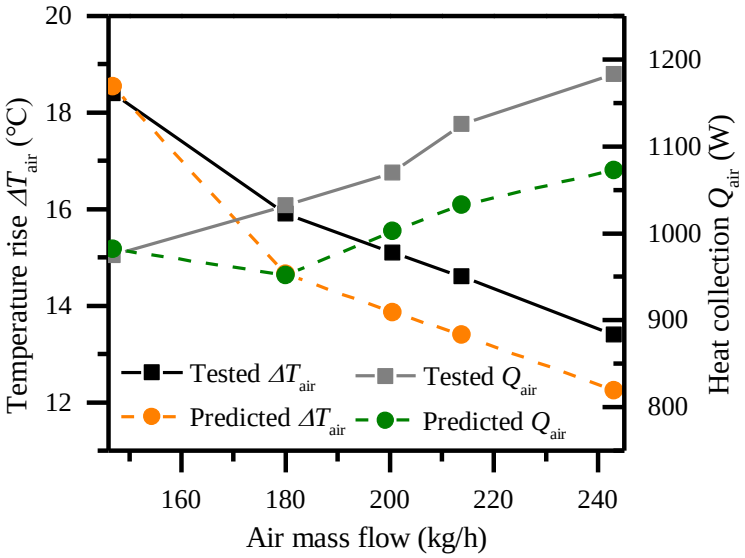

(b)

Fig. 6. The comparison between tested and predicted results at different mass flow

4. Result and discussion

4.1. Optical efficiency

Fig. 7 shows the solar radiation absorbed by absorber of TSAC_1 and TSAC_2 at 11:00, and the horizontal and vertical coordinates are consistent with Fig.2. The

absorbed solar radiation is divided into three regions from the top to the bottom, as the inclination angles of the absorbers are different. The absorbed solar radiation of TSAC_1 is lower on area 1 and higher on area 2 and 3, as the insulation material on the east side of TSAC_1 shields the solar radiation of area 1, while the insulation material on the west side reflects solar radiation to area 2 and 3. Similarly, due to the reflection of solar radiation from the bottom and back insulation materials, the solar radiation of TSAC_2 on areas 4, 5 and 6 is higher than other absorber positions.

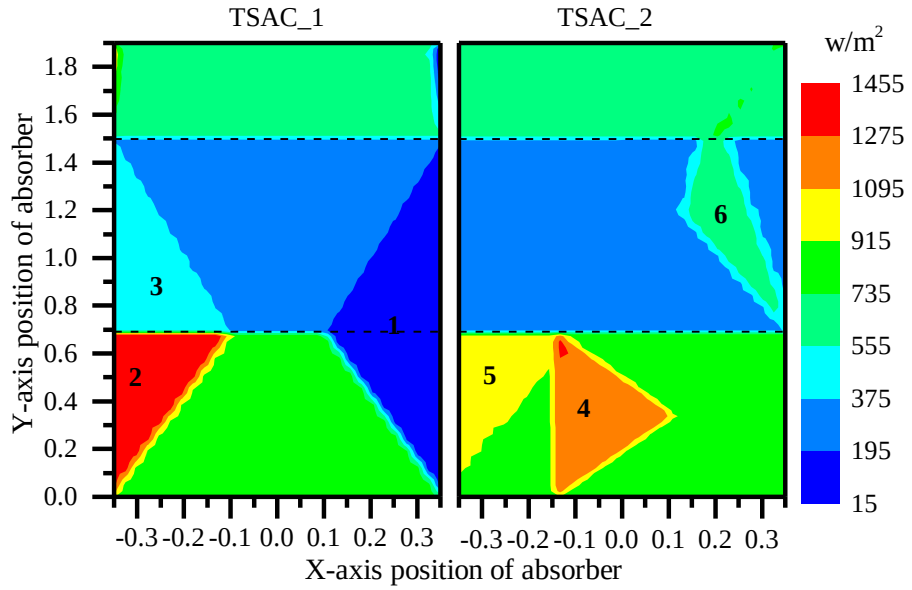

Fig. 7. The solar radiation absorbed by absorbers

The optical efficiency indicates the potential of solar collector to absorb solar radiation, and the thermal efficiency indicates the potential of solar collector to convert solar radiation, as the optical efficiency and thermal efficiency should be positively correlated. Based on the typical daily meteorological parameters of Tianjin, China (39.98°N, 117.38°E), the optical efficiency and thermal efficiency of TSAC_2 with insulation material absorption of 0.2 and 0.8 are calculated, respectively. As shown in Fig. 8, with the absorption of insulation material changing from 0.2 to 0.8, the η_{o1}

decreases, as the solar radiation absorbed by the absorber reduces. While the change of η_{o2} is consistent with that of thermal efficiency, which increases before 10:15 and after 14:40, and is almost unchanged at other times, as the higher absorption of insulation material reduces the solar radiation escaping from TSAC by insulation material reflection, when the incident angle is large. This indicates that η_{o2} is more reasonable to evaluate the optical properties of TSAC.

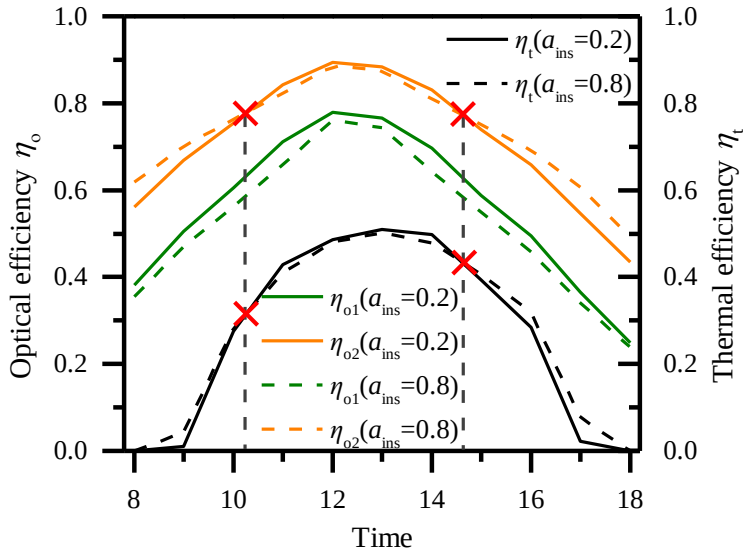

Fig. 8. The comparison of two optical efficiencies

The changes of η_{o2} and incident angle of three TSACs on typical day are shown in Fig. 9, and the variation trend of incident angle and optical efficiency is opposite with time. At 12:00, the incident angle is minimal, the solar radiation is almost all received by the absorber, and the optical efficiency is maximum as the absorber has high absorption. At other times, the incident angle increases, the proportion of solar radiation absorbed by the absorber decreases and more solar radiation escapes from TSAC, and the optical efficiency decreases. The average optical efficiency of the three TSACs is 55.8%, 71.0% and 68.5%, respectively. The TSAC_2 and TSAC_3 have superior

optical efficiency. The lower optical efficiency of TSAC_3 is due to the small transmittance of the side double transparent cover plate. The optical efficiency difference of the three TSACs is the smallest at 12:00, and the TSAC_2 is 7.0% and 1.0% larger than TSAC_1 and TSAC_3, as the direct solar radiation entering the three TSACs from the front transparent cover plate is the same at 12:00, the difference in optical efficiency is mainly caused by the diffuse radiation entering from the side transparent cover plate, and the diffuse radiation only accounts for about 15% of the total radiation and has little effect on optical efficiency. The greatest difference of optical efficiency is 22.8% between TSAC_1 and TSAC_2 at 18:00, as the incident angle is the largest and the insulation material on the side of TSAC_1 blocks most of the direct radiation.

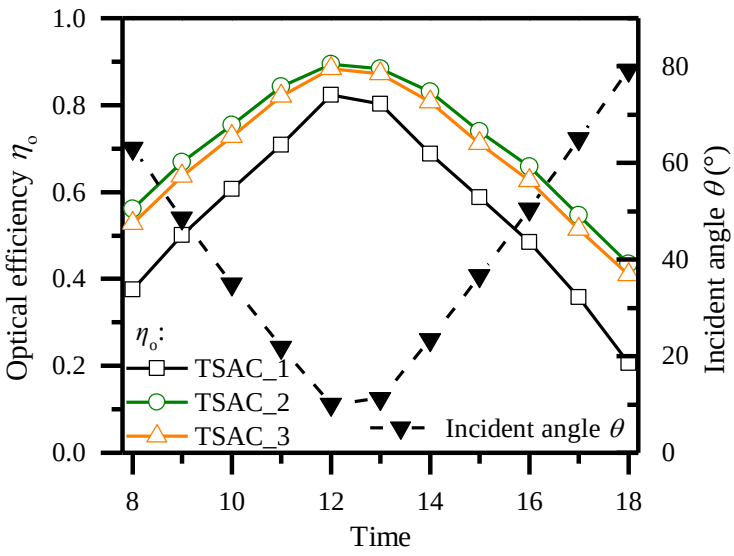

Fig. 9. The comparison of optical efficiency between three TSACs

4.2. Thermal efficiency

Environment temperature and global solar radiation are the key parameters affecting the thermal performance of TSAC. In addition, compared with traditional flat-

plate solar air collectors, TSAC has larger side areas and the insulation material can receive more solar radiation, as the solar azimuth angle and the absorption of the insulation material need to be considered. The effect of the above four key parameters on the thermal performance of TSAC was investigated, and the standard values of each parameter were set as follows: T_{env} = 0 ℃, I_{gc} = 605 W/m^2, β = 35°, a_{ins} = 0.2.

The effect of environment temperature on the thermal performance of the three TSAC is shown in Fig. 10. With the increase of environment temperature, the thermal loss of TSAC decreases, and the outlet temperature and thermal efficiency increase. TSAC_2 has the lowest average thermal efficiency as it has the greatest heat loss to the environment from the transparent cover plate on both sides, but due to the highest optical efficiency, its thermal efficiency increases fastest. The thermal efficiency of TSAC_1 is the highest when the environment temperature is below 0 ℃, otherwise the thermal efficiency of TSAC_3 is the highest, since the double transparent cover plate on both sides of TSAC_3 has higher optical efficiency and thermal resistance. Therefore, TSAC_1 is suitable for locations with low environment temperature, while TSAC_2 and TSAC_3 are opposite.

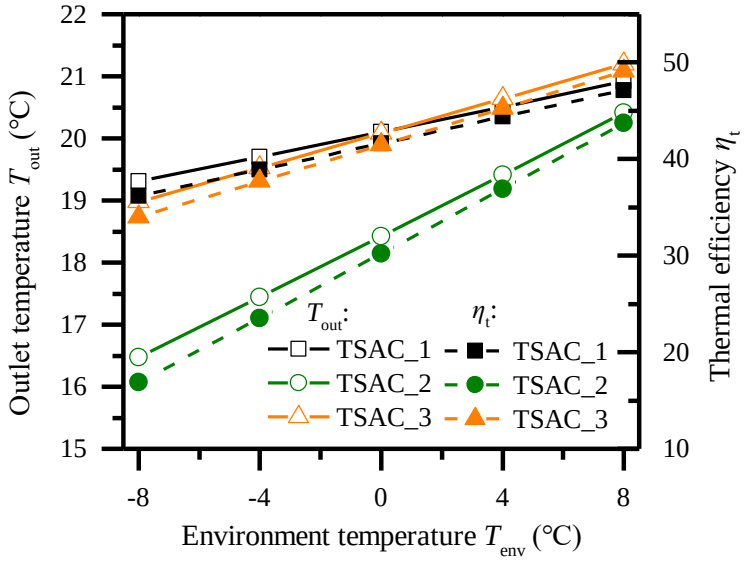

Fig. 10. The effect of environment temperature on the TSAC thermal performance

Fig. 11 shows the effect of global solar radiation on the thermal performance of the three TSACs. With the increase of global solar radiation, the outlet temperature and thermal efficiency rise, but the total solar radiation received by TSAC increases, and the thermal efficiency increases slowly. The optical efficiency of TSAC_2 and TSAC_3 is larger, and the outlet temperature and thermal efficiency increase faster than that of TSAC_1. When the solar radiation is higher than 600 W/m^2, the outlet temperature and thermal efficiency of TSAC_3 are greater than that of TSAC_1. This indicates that TSAC_2 and TSAC_3 have advantage at higher solar radiation.

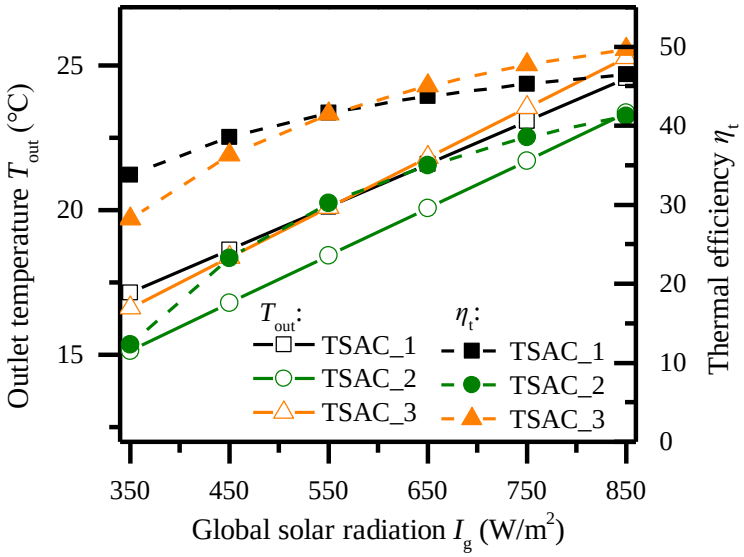

Fig. 11. The effect of global solar radiation on the TSAC thermal performance

The effect of solar azimuth angle on the thermal performance of the three TSAC is shown in Fig. 12. with the solar azimuth increases, the solar radiation received by the front transparent cover plate decreases, and the outlet temperature and thermal efficiency of TSAC_1 decrease rapidly. The outlet temperature of TSAC_2 and TSAC_3 increases first and then decreases, as the total solar radiation received by the front and side transparent covers plate of TSAC_2 and TSAC_3 is largest when the solar azimuth angle is about 25°. The side transparent covers plate of TSAC_2 and TSAC_3 can receive solar radiation resulting in the outlet temperature and thermal efficiency decreasing slowly. When the solar azimuth angle is greater than 40°, the outlet temperature and thermal efficiency of TSAC_3 are higher than that of TSAC_1. Therefore, TSAC_2 and TSAC_3 can receive more solar radiation in the morning and afternoon, and may have a greater heat collection.

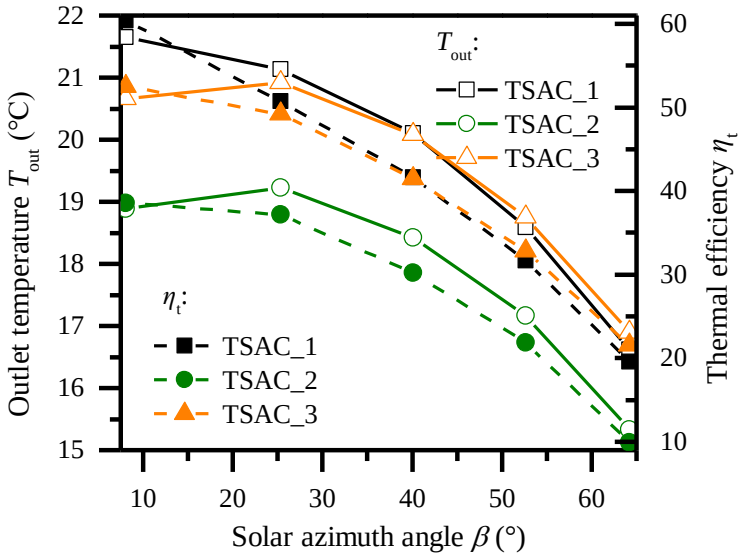

Fig. 12. The effect of solar incident angle on the TSAC thermal performance

Fig. 13 shows the effect of insulation material absorption on the thermal performance of the three TSACs. The insulation material of TSAC_1 receives little solar radiation as it only has a front transparent cover plate, and the outlet temperature and thermal efficiency of TSAC_1 remain constant under different insulation material absorption. The outlet temperature and thermal efficiency of TSAC_2 and TSAC_3 increase with the rise of insulation material absorption, as insulation material with higher absorption can improve their optical efficiency. The low transmittance of the double transparent cover plate on the side of TSAC_3 leads to less solar radiation received by its insulation material, and the thermal efficiency rises more slowly than that of TSAC_2, and thus the TSAC_2 can improve its thermal efficiency by coating an absorption layer to the surface of insulation material.

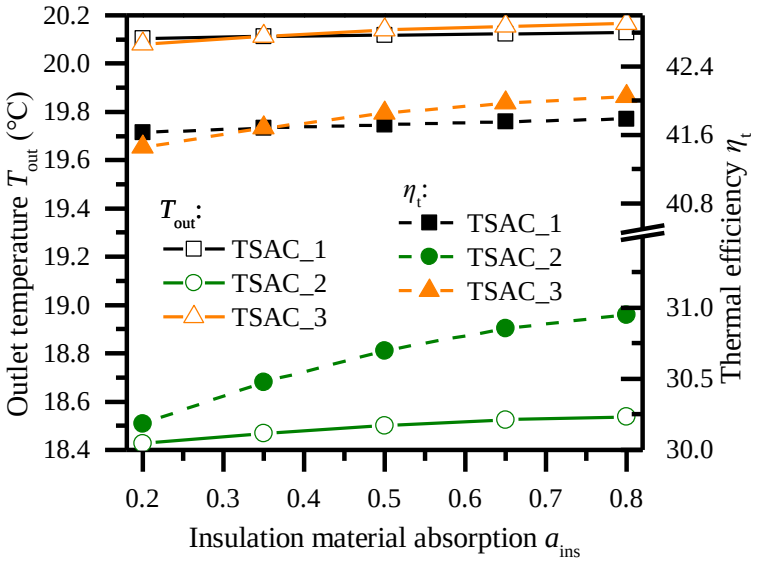

Fig. 13. The effect of insulation absorptivity on the TSAC thermal performance

4.3. Heat collection in different regions

Environmental parameters have a great impact on the thermal performance of TSAC, as it is necessary to analyze the applicability of the TSAC in different climatic regions and different solar energy distribution regions. China has five climatic regions and four solar energy distribution regions, which are divided according to the average temperature of the coldest month (T_{min}) and the total annual radiation (I_{year}), respectively, as shown in the Table 3 (Fan et al., 2018). With these two divisions, eight cities are selected and their location, classification information, and climatic details are depicted in fig. 13 (a), and Table 4.

Fig. 14 (b) shows the heat collection and average thermal efficiency of three TSACs during the whole heating period. TSAC_1 with insulation material on both sides is suitable for severe cold regions, as it has less heat loss to the environment by the transparent cover plate, and the heat collection of TSAC_1 in Hohhot and Shenyang is 40% higher than that of TSAC_2, and the average thermal efficiency is 34.9%. On the

contrary, TSAC_2 is suitable for temperate and warm-winter regions, its average thermal efficiency in Xiamen, Kunming and Chuxiong is 59.9%, and 10.1% higher than that of TSAC_1. TSAC_3 is suitable for cold and cold-winter regions, and the maximum heat collection is 4176.6 MJ in Lasa. In addition, the heat collection of TSAC_3 in Shijiazhuang is 1623.5 MJ, and compared with the traditional flat-plate solar air collectors with the same perforated corrugated absorber (Zheng et al., 2016), the heat collection is increased by 24.3% under the same installation area. The TSAC with the highest heat collection in each city is shown in Fig. 13 (a), and the average thermal efficiency of the optimal TSAC in the eight cities can reach 47.3%, which is 5.4% higher than that of TSAC_1.

Table. 3. Climatic regions and soler energy distribution regions.

Category	Classification	Major index
Climatic regions	Severe cold	$T_{min} \leq$ -10 ℃
	Cold	-10 ℃ < $T_{min} \leq$ 0 ℃
	Hot-summer and cold winter	0 ℃ < $T_{min} \leq$ 10 ℃
	Hot-summer and warm winter	T_{min} > 10 ℃
	Temperate	0 ℃ < $T_{min} \leq$ 13 ℃
Solar energy distribution regions	Rich	$I_{year} \geq$ 6700 MJ/m^2
	Relatively rich	5400 MJ/m^2 $\leq I_{year} <$ 6700 MJ/m^2
	Available	4200 MJ/m^2 $\leq I_{year} <$ 6700 MJ/m^2
	Absent	$I_{year} <$ 4200 MJ/m^2

Table. 4. Meteorological parameters of 8 cities.

City	T_{min}	I_{year} (about)(MJ/m^2)	Humidity	Altitude (m)
Lasa	-8℃ ~ 8℃	7473.3	28%	3648.7
Shenyang	-18℃ ~ 8℃	4965.5	60%	44.7

Hohhot	-15℃ ~ 5℃	6241.2	58%	1063.0
Shijiazhuang	-6℃ ~ 3℃	5368.0	55%	81
Xiamen	11℃ ~ 18℃	5066.8	79%	139.4
Chengdu	3℃ ~ 10℃	3347.2	83%	506.1
Kunming	3℃ ~ 17℃	5430.0	68%	1892.4
Chuxiong	4℃ ~ 17℃	6571.0	75%	1772

(a)

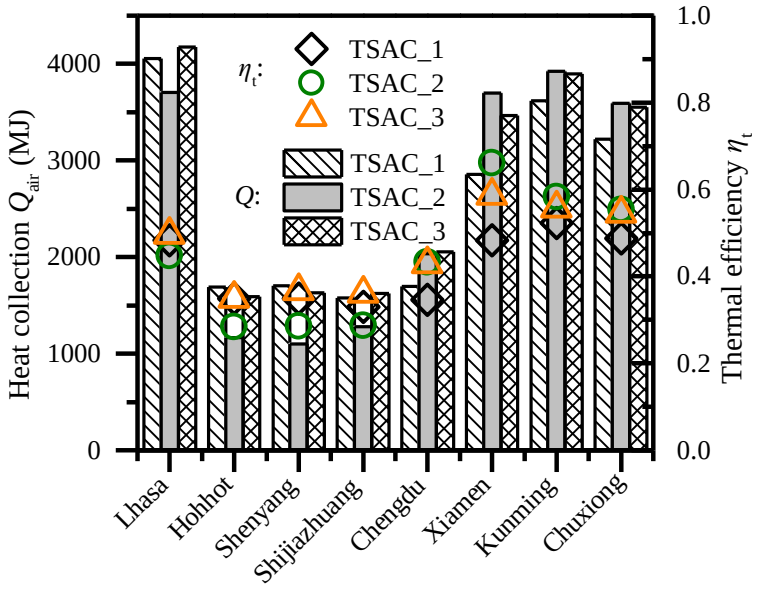

(b)

Fig. 14. The heat collection of TSAC during heating period in different regions

In some cities, the solar radiation in the afternoon is much higher than that in the morning. Under this condition, TSAC_1 and TSAC_2 can be combined into TSAC_4, the east side of TSAC_4 is an insulation material, and the west side is a transparent cover plate. Fig. 15 shows the hourly heat collection comparison of TSAC_2 and TSAC_4 under a typical day in Kunming. The noon of local solar time is about 13:00, and the average solar radiation in the morning is only 430.3 W/m^2, while that in the afternoon is 625.3 W/m^2. The insulation material on the east side of TSAC_4 will waste some solar radiation in the morning, but reduces its heat loss and improves thermal efficiency throughout the day, and the higher solar radiation in the afternoon is fully utilized by the transparent cover plate on the west side. The heat collection of TSAC_2 is 1.5 MJ higher than that of TSAC_4 in the morning, but 2.4 MJ lower than that of TSAC_4 throughout the day. During the heating period, the total heat collection of TSAC_4 is 7.5% higher than that of TSAC_2, and TSAC_4 replaces TSAC_2 as the optimal TSAC in Kunming.

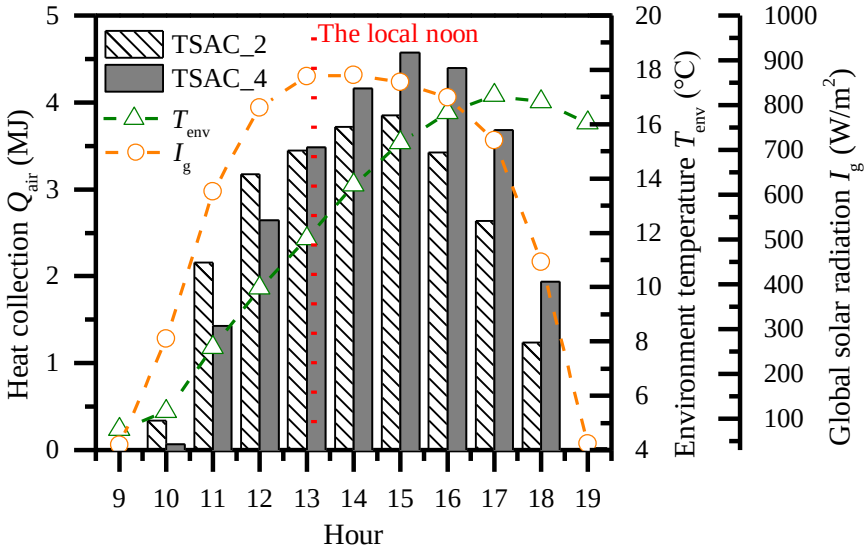

Fig. 15. The applicability of TSAC with single side transparent cover plate

4.4. Economic and environmental impacts

Fig. 16 shows the LCC and LCOH of the three TSACs in eight regions, and the economic parameters of three TSACs are presented in Table. 5. The LCC of TSAC_1, TSAC_2 and TSAC_3 is 177.1 $, 189.2 $ and 221.2 $ respectively, as the price of the transparent cover plate is higher than the insulation material. The different heat collection of TSACs in the eight regions leads to the LCOH changes. In general, LCOH is higher in severe cold and cold regions due to large heat loss and small heat collection, while the LCOH of Lhasa as a cold region is lowest because of its rich solar energy. The TSAC_1 has economic advantages in Lhasa, Hohhot, Shenyang and Shijiazhuang, while TSAC_2 has economic advantages in other cities. TSAC_3 has no economic advantages in the eight cities due to its high LCC. Select the TSAC with the best economy in eight cities, the average LCOH is 0.012 $/kWh, and less than one-sixth of the electricity price 0. 0751 $/kWh.

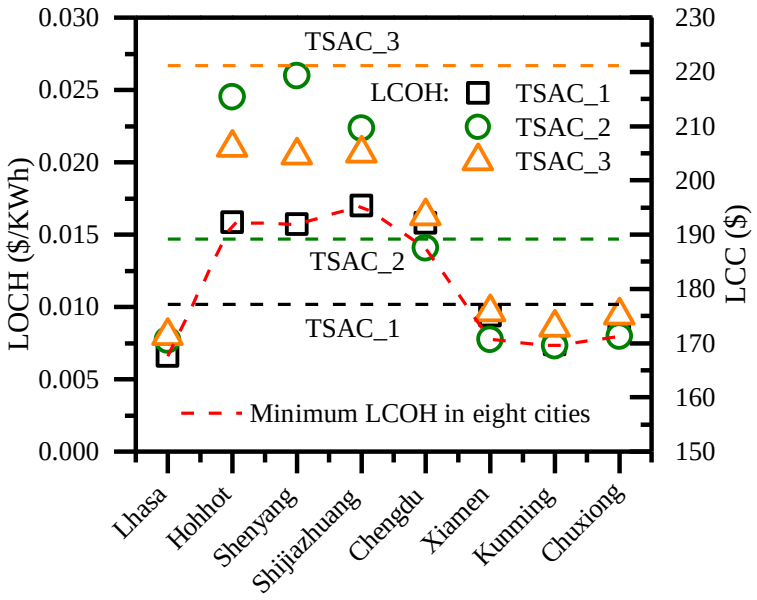

Fig. 16. The life cycle economic of TSACs

Table. 5. The economic parameters of TSACs.

Parameter	Value
IC of TSAC_1	58.8 $/m^2
IC of TSAC_2	65.2 $/m^2
IC of TSAC_3	82.4 $/m^2
MC	10% of annual cost
SV	5% of *IC*
Electric power cost	0.075 $/(kWh)
Fan power	30W
n	20 years

Fig. 17 shows the CO_2 emission reduction of the TSAC with the largest heat collection in each region based on the whole life cycle. The material consumption of 1 m^2 TSAC and CO_2 emission factors are presented in Table. 6. $RTCO_2$ is the total CO_2 emission reduction by TSAC heat collection, and its maximum value is 6331.7 kg of TSAC_3 in Lhasa. $EECO_2$ of TSACs in different regions is certain, as TSACs have the same operation time, and if the generation of 1 kWh electricity emits 2 kg of CO_2, the $EECO_2$ of TSACs is 1440 kg. $EPCO_2$, $ETCO_2$ and $RDCO_2$ are less than $EECO_2$ and have the same value for the specified TSAC, and the sum of them to TSAC_1, TSAC_2

and TSAC_3 is 232.5 kg, 165.7 kg and 181.3 kg, respectively. $RNCO_2$ has the same trend as $RTCO_2$, and the average $RNCO_2$ in eight regions is 3230.3 kg.

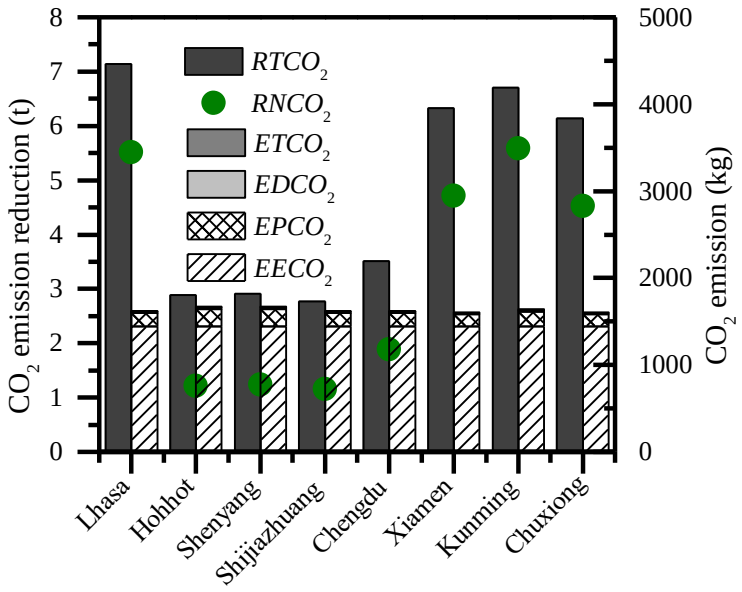

Fig. 17. The life cycle CO_2 emission reduction of TSACs

Table. 6. The material consumption of 1 m^2 TSAC and CO_2 emission factors.

Material	TSAC_1	TSAC_2	TSAC_3	TSAC_4	EF_{pro}	EF_{tran}
Polycarbonate	4.1 kg	11.9 kg	3.8 kg	18.7 kg	1.1	0.15
Stainless steel	10.1 kg	11.9 kg	1.8 kg	9.0 kg	2.3	0.15
Polystyrene board	16.0 kg	11.9 kg	3.8 kg	9.0 kg	5.0	0.15
Galvanized sheet	7.1 kg	11.9 kg	2.8 kg	13.9 kg	2.8	0.15

5. Conclusions

A novel triangular solar air collector (TSAC) is proposed and its structure is modified to adapt to different climatic regions. The finite volume optical model and dynamic heat transfer model of TSACs were established and coupled, and the mesh independence test and experimental verification of the numerical model were carried out. The optical efficiency, thermal efficiency, heat collection in eight different climates

and solar energy distribution cities, and life-cycle economics and CO_2 emission reduction of different TSAC structures were compared and analyzed. The main conclusions are drawn as follows:

(1) The optical efficiency 2 is more reasonable as solar radiation absorbed by transparent cover plate and insulation material is considered, and the TSAC with sides transparent cover plate (TSAC_2) has the highest daily average optical efficiency of 71.0%, and 15.2% higher than that of TSAC with sides insulation material (TSAC_1).

(2) TSAC_2 has the advantage of higher solar radiation and environment temperature, while TSAC_1 is the opposite. The absorption of insulation material has a great effect on TSAC_2, and its thermal efficiency increases by about 1% with the insulation material absorption rising from 0.2 to 0.8.

(3) TSAC_1 is suitable for severe cold regions, TSAC_2 is suitable for temperate and warm-winter regions, and TSAC with sides double transparent cover plate (TSAC_3) is suitable for cold and cold-winter regions. During the heating period, the average thermal efficiency of the optimal TSAC in eight cities is 47.3%, and the maximum heat collection is 4176.6 MJ in Lasa.

(4) The average LCOH of TSACs in eight cities is 0.012 $/kWh, and less than one-sixth of the electricity price, and the average $RNCO_2$ based on the whole life cycle is 3230.3 kg.

Results of this study contributes to promoting the application of TSAC in different climatic regions. In our future works, the absorber structure of the TSAC will be

optimized to improve its optical and thermal properties, and the heat collection performance, economy and CO_2 emission reduction ability of optimal TSAC and traditional flat-plate solar air collector will be compared and analyzed in different regions.

Acknowledgement

This work was supported by the National Key R&D Program of China (No. 2020YFD1100304).

References

Bejan A.S., Croitoru C., Bode F., Teodosiu C., Catalina T., 2022. Experimental investigation of an enhanced transpired air solar collector with embodied phase changing materials. Journal of Cleaner Production, 336, 130398.

http://dx.doi.org/10.1016/j.jclepro.2022.130398

Chand S., Chand P., Kumar Ghritlahre H., 2022. Thermal performance enhancement of solar air heater using louvered fins collector. Solar Energy, 239, 10-24.

http://dx.doi.org/10.1016/j.solener.2022.04.046

China National Energy Administration, 2022. 2022 Renewable Energy Report of China, http://www.nea.gov.cn/, [assessed 17 June 2022]

Dong Z., Chang L., Jianjun Z., Jinlong J., Zhoujian A., Linjun W., 2021. Thermal economic analysis of a double-channel solar air collector coupled with draught fan: Based on energy grade. Renewable Energy, 170, 936-947.

http://dx.doi.org/10.1016/j.renene.2021.02.051

Fan M., Liang H., You S., Zhang H., Yin B., Wu X., 2018. Applicability analysis of the solar heating system with parabolic trough solar collectors in different regions of China. Applied Energy, 221, 100-111.

https://doi.org/10.1016/j.apenergy.2018.03.137

Fan M., You S., Gao X., Zhang H., Li B., Zheng W., et al., 2019. A comparative study on the performance of liquid flat-plate solar collector with a new V-corrugated absorber. Energy Conversion and Management, 184, 235-248.

http://dx.doi.org/10.1016/j.enconman.2019.01.044

Gao M, Wang D, Liu Y, Wang Y, Zhou Y, 2020. A study on thermal performance of a novel glazed transpired solar collector with perforating corrugated plate. Journal of Cleaner Production, 257, 120443.

http://dx.doi.org/10.1016/j.jclepro.2020.120443

Jiang Y., Zhang H., Wang Y., You S., Wu Z., Fan M., Wang L., Wei S., 2021. A comparative study on the performance of a novel triangular solar air collector with tilted transparent cover plate. Solar Energy 227, 224-235.

https://doi.org/10.1016/j.solener.2021.08.083

Jiang Y., Zhang H., Zhao R., Wang Y., Liu M., You, S., Wu Z., Liu Z., Wei S., 2022. Research on the operation strategies of the solar assisted heat pump with triangular solar air collector. Energy 246, 123398.

https://doi.org/10.1016/j.energy.2022.123398

Kareem M.W., Habib K., Pasha A.A., Irshad K., Afolabi L.O., Saha B.B., 2022.

Experimental study of multi-pass solar air thermal collector system assisted with sensible energy-storing matrix. Energy, 245, 123153.

http://dx.doi.org/10.1016/j.energy.2022.123153

Ke W., Ji J., Xu L., Xie H., Wang C., Yu B., 2021. Annual performance analysis of a dual-air-channel solar wall system with phase change material in different climate regions of China. Energy, 235, 121359.

http://dx.doi.org/10.1016/j.energy.2021.121359

Khanlari A., Sozen A., Tuncer A.D., Afshari F., Gurbuz E.Y., Bilge Y.C., 2021a. Numerical and experimental analysis of longitudinal tubular solar air heaters made from plastic and metal waste materials. Heat Transfer Research, 52, 19-45.

http://dx.doi.org/10.1615/HEATTRANSRES.2021038204

Khanlari A., Sözen A., Afshari F., Tuncer A.D., Ağbulut Ü., Yılmaz Z.A., 2021b. Numerical and experimental analysis of parallel-pass forced convection solar air heating wall with different plenum and absorber configurations. International Journal of Numerical Methods for Heat & Fluid Flow, 32.

http://dx.doi.org/10.1108/HFF-03-2021-0160

Kizildag D., Castro J., Kessentini H., Schillaci E., Rigola J., 2022. First test field performance of highly efficient flat plate solar collectors with transparent insulation and low-cost overheating protection. Solar Energy, 236, 239-248.

http://dx.doi.org/10.1016/j.solener.2022.02.007

Liang H., Zhu C., Fan M., You S., Zhang H., Xia J., 2018. Study on the thermal

performance of a novel cavity receiver for parabolic trough solar collectors. Applied Energy, 222, 790-798.

http://dx.doi.org/10.1016/j.apenergy.2018.04.030

Marc O., Praene J., Bastide A., Lucas F., 2010. Modeling and experimental validation of the solar loop for absorption solar cooling system using double-glazed collectors. Applied Thermal Engineering, 31, 268-277.

http://dx.doi.org/10.1016/j.applthermaleng.2010.09.006

Ramasamy A.K., Ganesh M., Rajamani K., Loganathan A.K., Rangaswamy R., 2021. Investigation of concentrated solar collector with discretized flat mirrors in parabolic arrangement.Energy for Sustainable Development, 64, 25-34.

http://dx.doi.org/10.1016/j.esd.2021.07.005

Rani P., Tripathy P.P., 2022. Experimental investigation on heat transfer performance of solar collector with baffles and semicircular loops fins under varied air mass flow rates.International Journal of Thermal Sciences, 178, 107597.

http://dx.doi.org/10.1016/j.ijthermalsci.2022.107597

Renewable Energy International Agency. Solar Installed Capacity Report of China,https://www.irena.org/solar;2022[assessed 17 June 2022]

Tuncer A.D., Sözen A., Khanlari A., Amini A., Şirin C., 2020. Thermal performance analysis of a quadruple-pass solar air collector assisted pilot-scale greenhouse dryer. Solar Energy, 203, 304-316.

http://dx.doi.org/10.1016/j.solener.2020.04.030

Ur Rehman N., 2018. Optical-irradiance ray-tracing model for the performance analysis and optimization of a façade integrated solar collector with a flat booster reflector. Solar Energy, 173, 1207-1215.

http://dx.doi.org/10.1016/j.solener.2018.07.096

Vengadesan E., Senthil R., 2020. A review on recent developments in thermal performance enhancement methods of flat plate solar air collector. Renewable and Sustainable Energy Reviews, 134, 110315.

http://dx.doi.org/10.1016/j.rser.2020.110315

Zhang H., Ma X., You S., Wang Y., Zheng X., Ye T., et al., 2018. Mathematical modeling and performance analysis of a solar air collector with slit-perforated corrugated plate. Solar Energy, 167, 147-157.

http://dx.doi.org/10.1016/j.solener.2018.04.003

Zhang Y., Liu Z., Wu Z., Zhang L., Luo Y., 2019. Numerical evaluation on energy saving potential of the photovoltaic fresh air preheating system in different climate regions of China. Applied Thermal Engineering, 154, 407-418.

http://dx.doi.org/10.1016/j.applthermaleng.2019.03.108

Zheng W., Li B., Zhang H., You S., Li Y., Ye T., 2016. Thermal characteristics of a glazed transpired solar collector with perforating corrugated plate in cold regions. Energy, 109, 781-790.

http://dx.doi.org/10.1016/j.energy.2016.05.064

Zhao R., Zhao L., Deng S., Zheng N., 2015. Trends in patents for solar thermal

utilization in China. Renewable and Sustainable Energy Reviews, 52, 852-862.

http://dx.doi.org/10.1016/j.rser.2015.07.181

Zhao Y., Meng T., Jing C., Hu J., Qian S., 2020. Experimental and numerical investigation on thermal performance of PV-driven aluminium honeycomb solar air collector. Solar Energy, 204, 294-306.

http://dx.doi.org/10.1016/j.solener.2020.04.047